Scalable method for micro-CT analysis enables large scale quantitative characterization of brain lesions and implants

David B. Kastner[1,2*], Viktor Kharazia[2*], Rhino Nevers[2], Daniela Astudillo Maya[2], Greer M. Williams[1], Zhounan Yang[1], Clay Smyth[2], Luca Della Santina[3], Dilworth Y. Parkinson[4], Loren M. Frank[2,5]

[1]*Department of Psychiatry, University of California, San Francisco, CA 94143, USA*

[2]*Kavli Institute for Fundamental Neuroscience and Department of Physiology, University of California, San Francisco, CA 94158, USA*

[3]*Deparment of Ophthalmology, University of California, San Francisco, CA 94143, USA*

[4]*Advanced Light Sources Division, Lawrence Berkeley National Labs, Berkeley, CA 94720, USA*

[5]*Howard Hughes Medical Institute*

[*]*These authors contributed equally to this work*

Corresponding author: David B. Kastner, david.kastner2@ucsf.edu

Abstract

Anatomic evaluation is an important aspect of many studies in neuroscience; however, it often lacks information about the three-dimensional structure of the brain. With appropriate contrast, micro-CT imaging provides an excellent, nondestructive, method for the evaluation of brain structure, but currently available protocols are labor intensive, use hazardous compounds, complicate standard histological analysis, and require the removal of the skull. Here we present a simple protocol that solves those problems. We use eosin in combination with bone decalcification to create contrast in the tissue and then employ monochromatic and propagation phase-contrast micro-CT imaging to enable the imaging of brain structure with the preservation of the surrounding skull. Instead of relying on descriptive, time-consuming, or subjective methods, we develop simple quantitative analyses to map the locations of recording electrodes and to characterize the presence and extent of brain lesions.

Introduction

Evaluating brain structure presents a critical confirmatory step for much of systems neuroscience. This often occurs through histological sectioning and light-microscopic analysis. Although such a technique provides a high-resolution view of brain structures, it is time-consuming, difficult to scale for high-throughput analyses, and, perhaps most problematic, it destroys the three-dimensional structure of the brain. Additionally, histological processing is often accompanied by description analyses and not quantitative evaluation. Newer, tissue clearing, methods (Chung et al., 2013; Renier et al., 2014) maintain the three-dimensional structure of the brain for high resolution imaging, but remain expensive, labor intensive, and not well equipped to evaluate lesions or electrode localization, mainstays of systems neuroscientific inquiry. Micro-CT presents an excellent middle ground for evaluating brain anatomy while maintaining three-dimensional structure (Ding et al., 2019; Dyer et al., 2017; Masís et al., 2018).

A previous, elegant, protocol was developed for micro-CT imaging of the post-mortem rodent brain (Masís et al., 2018); however, that protocol, although clear and well described, contains many involved steps, some of which require expensive and hazardous elements, including osmium. There is no evidence that that protocol could work if the skull was left intact, and simple quantitative methods for the analysis of the imaged volume were not established. Furthermore, in using osmium, it becomes far more challenging to process the brain for subsequent standard histologic techniques, requiring a decision to be made between either imaging the full three-dimensional volume, or using standard histologic processing.

Drawing upon the soft-organ literature (Busse et al., 2018; Müller et al., 2018) we present an easy, scalable and inexpensive protocol for providing contrast to the post-mortem brain using eosin as the contrast agent. Furthermore, we adapt decalcification techniques (Hatta et al., 2014; Savi et al., 2017) to image the brain with critical parts of the skull intact. To extract maximal contrast from the brain, we scan the brain with monochromatic X-rays and propagation phase contrast imaging, both of which benefit from utilizing a synchrotron source for the X-rays. The resulting protocol is simple and allows for evaluation of brain structure

relative to the coordinates determined by skull sutures. It does not preclude further processing with standard histologic techniques. In addition, we present quantitative methods to localize electrodes within the brain and describe the extent of lesions within the brain.

Material and Methods

Animals: All experiments were conducted in accordance with University of California, San Francisco Institutional Animal Care and Use Committee and US National Institutes of Health guidelines. Datasets were collected from male Long-Evans rats that were fed standard rat chow (LabDiet 5001).

Surgery: Anesthesia was induced using ketamine, xylazine, atropine, and isoflurane. For the animals that underwent surgery, they were either implanted with a multielectrode microdrive, or underwent lesioning of the dorsal and intermediate hippocampus. For the microdrive implant, craniotomies and accompanying durotomies were placed at +2.6 ML and -4.0 AP for the dorsal hippocampal canula and +4.7 ML and -5.7 AP for the intermediate hippocampal canula. Values are relative to bregma. Screws were imbedded into the skull to support the acrylic casing that secured the microdrive onto the skull of the rat. For the lesion rats, craniotomies were drilled bilaterally to allow for access to all 24 injection sites (Table 1) and the injection needle (33 gauge) was inserted through the dura. For each lesion site, the needle was lowered 0.1 mm below the target coordinates and then raised back to the target prior to injection. 120 nl of NMDA (10 mg/ml) was injected at each site at a rate of 0.1 µl/min. The needle was left at the site for 2 minutes after finishing the injection. For the rats that underwent control surgeries, everything was the same as the lesion rats, except no NMDA was injected, and the needle did not dwell at the hypothetical injection site. The animals that underwent the lesion surgery (either with or without injection of the NMDA) received Diazepam 10 mg/kg intraperitoneally post-operatively.

Electrophysiological recording: Tetrodes were individually moved toward the hippocampus daily. Physiological data, digitized at 30 kHz, and was recorded using the SpikeGadgets data acquisition system and the Trodes software package (SpikeGadgets).

Processing for micro-CT: Prior to perfusion, animals were anesthetized with isoflurane, and then euthanized with pentobarbital. Animals were perfused intracardially with 100 mL of phosphate buffer solution (PBS), followed by 250 mL of chilled 4% paraformaldehyde in PBS. The skull was dissected out with the brain intact, with most of facial bones trimmed off, and all soft tissues removed. A 5-mm-wide opening was made using a rongeur on the ventral side along the midline (optional), for improved diffusion of fixative. The sample was then placed in 50mL of the same fixative for 48 hours at 4°C.

Subsequently, the sample was rinsed in PBS with 0.05% sodium azide (PBS-azide) and decalcified by placing it in a container with 250 mL of 8% EDTA (Sigma-Aldrich) for 6-7 days at room temperature on an orbital shaker. The solution was replaced once midway through the decalcification.

After rinsing again in PBS-azide, the decalcified skull was further trimmed to a final size on both anterior and posterior sides using a razor blade. Care was taken to avoid compressing or otherwise distorting the brain. The trimmed sample was placed in 50mL of 5% Eosin Y (Sigma-Aldrich) for 6-7 days at 4°C on an orbital shaker. The solution was replaced once after 48 hours. The sample was then rinsed in PBS and stored in 50mL PBS-azide at 4°C prior to micro-CT scanning.

For Nissl staining, the brain (with skull removed) was cut using a Vibratome 3000 (Leica Biosystems); 50-80 um thick coronal sections were collected into a 24-well dish with PBS-azide and stored at 4°C. Sections were mounted on adhesive slides, air-dried, and stained using a traditional cresyl violet staining protocol.

Micro-CT scanning and image reconstruction: Scanning was done at beamline 8.3.2 (tomography) at the Advanced Light Source (ALS) at Lawrence Berkeley National Laboratory (Fig S1). All scans were carried out at room temperature.

For the brain with the implanted microdrive, the brain anterior and posterior to the hippocampus were removed to decrease the width of the brain to maximize resolution for the imaging. Furthermore, as many as possible of the skull screws were removed to minimize interference. As the microdrive was still attached to the skull via acrylic and remaining skull screws, it provided the support for the brain. The brain was out of solution for the scanning. X-rays passed through the sample along the A-P/M-L axes as the sample rotated.

For the rest of the brains, the sample was placed snuggly in a conical tube and was not in solution (Fig S1). X-rays passed through the sample along the M-L/D-V axes as the sample rotated. This is the narrowest dimension of the brain, thereby allowing for the finest resolution ~7 µm/pixel (see Table 2).

Monochromatic X-rays were generated using a multilayer mirror monochromator. Energy of 25 keV was used, and the sample was placed 54 cm (maximal distance for beamline) from the collector (Fig S1) to enable maximal usage of propagation phase contrast imaging. A total of 1313 angles with an exposure time of 100 – 125 ms were used to collect the image (Table 2).

The images were reconstructed using tomopy using a script designed at the ALS (https://bitbucket.org/berkeleylab/als-microct-python/src/master/tomopy832/tomopy832.py). See Table 2 for the parameters used for the reconstruction of the various brains. Multiple tiles were manually stitched together to create the final imaged volume (Table 2).

Image visualization and analysis: Fiji (Schindelin et al., 2012; 2015; Schneider et al., 2012) was used to visualize virtual slices of the brain and to create a mask of the hippocampal region for the lesion analysis using the Segmentation Editor tools. Imaris (Oxford Instruments) was used for three-dimensional reconstruction of the brain. Slicer-3D 4.10.2 (https://www.slicer.org/) (Fedorov et al., 2012; Kikinis et al., 2014) was used to register and align the brains (http://hdl.handle.net/1926/1291) by finding the linear transformation (rotation and translation) to place the entirety of the imaged brains into a shared coordinate system. The alignment of the brains was not restricted to align any specific region of the brain (such as just the hippocampus) and rather worked to best align the whole brain and skull.

For the lesion analysis we were interested in understanding the similarity of the hippocampal formation between brains as that was the region of lesioning. Therefore, we created a mask for the left and right hippocampal region. The mask was intentionally generous to ensure that the entire hippocampal formation was included for all brains. For each virtual slice we found the similarity between all pairs of brains using the structural similarity metric (SSIM) (Wang and Bovik, 2009; Wang et al., 2004). For SSIM we used a gaussian smoothing filter for the images with a sigma of 50 pixels. A dendrogram that grouped lesioned and control brains was calculated using single-linkage hierarchical clustering over the average SSIM for all pairs of brains. The similarity matrix was subtracted from 1 to create a dissimilarity matrix as the input to the hierarchical clustering.

Theta phase offset calculation: The local field potential (LFP) was defined as the voltage from each tetrode after being low-pass filtered below 400 Hz and down-sampled to 1.5 kHz. To extract theta oscillations, the LFP data were band-pass filtered with a Parks-McClellan optimal equiripple FIR filter (pass band between 4 and 10 Hz, stop bands below 3 Hz and above 11 Hz) applied in both the forward and reverse directions to prevent phase distortion (Lubenov and Siapas, 2009). Instantaneous theta phase was calculated as the angle of the Hilbert-transformed theta oscillation.

Analysis of theta phase was limited to time periods when the rat was running, which was defined as a body speed greater than 10 cm/s (Lubenov and Siapas, 2009). Instantaneous phase differences between pairs of tetrodes were measured as the angle between the complex phase vectors for each tetrode. For each running period, the average pairwise phase difference was calculated as the circular mean over time of the angle between phase vectors, and the average phase offset over the entire behavior session was calculated as the circular mean of individual average phase differences for each running period.

Results:

Brain structure with intact skull

To utilize micro-CT for structural imaging of the brain it is critical to add a substrate to provide contrast to resolve different brain structures. In developing our protocol, our first goal was to create as simple a procedure as possible, and one that does not require osmication, dehydration of the tissue, nor imbedding in resin (Masís et al., 2018). We therefore developed a protocol wherein we use eosin (Busse et al., 2018) to provide contrast within the brain, and imaged the brain using monochromatic X-rays at the Advanced Light Source at Lawrence Berkeley National Lab. The monochromatic, lower energy, X-ray source is far less harsh than would be polychromatic white light, obviating the need for any further protective processing to the brain, even with the greater flux of X-rays provided by a synchrotron.

Typically, the skull would be removed to image the brain, as it provides a barrier for light transmission. However, the skull provides the reference frame for the stereotactic coordinates utilized to target specific brain structures while the animal is alive. Removing the dorsal skull therefore discards a piece of information critical for evaluating and refining anatomical targeting. Furthermore, the skull also provides a rigid structure to prevent alterations to the

brain dimensions due to histological processing. Therefore, in addition to processing the brain with eosin, we also adapted decalcification techniques to leave most of the skull in place but allow for enough transmitted X-rays to image the underlying brain.

With our method we are able to image the whole rat brain with the overlying skull (Fig 1 & Vid 1). The eosin provides sufficient contrast to the brain to allow for the visualization of many different brain regions. Given that the imaging provides a three-dimensional volume, we can virtually section the brain to any given region of interest along any plane of interest (Fig 1B). Having the skull intact allows for setting the frame of reference of the brain as one would in surgery by leveling bregma and lambda.

An advantage of using eosin to provide contrast to the brain is that it is commonly used stain for histology, and therefore still allows for classic histologic imaging following the micro-CT. Therefore, using the same brain, following the micro-CT, we sectioned the brain and stained it with Cresyl Violet to demonstrate the Nissl substance in the neurons. Nissl-stained brain sections exhibited well preserved morphology and can be used as anatomic reference to corresponding micro-CT virtual slices (Fig 2).

Lesion quantification

Lesions provide a useful perturbation for evaluating the necessity of brain regions for behavior. However, validating a lesion using sectioning, staining and imaging presents a challenge for quantification, often leading to more descriptive analyses. Therefore, we utilized our protocol to quantitatively evaluate the presence and extent of hippocampal lesions.

The CT protocol enables clear visualization of the lesioned area of the brain (Fig 3A). Quantification of the lesion could be done by image segmentation, as was done with previous micro-CT processing (Masís et al., 2018); however, image segmentation is laborious and prone to subjectivity. Therefore, we sought a more automatable and objective approach for quantifying the presence and extent of lesions.

We processed and collected micro-CT images of 25 rat brains—12 rats underwent control surgery and 13 rats underwent hippocampal lesion surgery (see Material and Methods). We aligned all brains to a common reference and created a mask to extract the three-dimensional region of the hippocampus across all brains (Fig 3B). We calculated the similarity of all pairs of brains for each virtual slice using SSIM (Fig 3C), a similarity metric designed to capture the perceptual similarity between images (Wang et al., 2004; Wang and Bovik, 2009). We clustered the brains using hierarchical clustering based on the average pairwise similarity matrix across the bilateral dorsal hippocampal formation and bilateral dorsal-most portion of the intermediate hippocampal formation (the portion of the hippocampal formation that was lesioned (Table 1)). The lesion and control brains separate into different groups by the clustering (Fig 3D).

To visualize the extent of the lesion, for all brains and virtual slices we found the most similar control brain and then plotted those values for the group of control and lesion brains across the dorsal and intermediate/ventral hippocampus for both the left and right sides of the brain (Fig 3E). Across the entire extent of the dorsal hippocampus, and the initial part of the intermediate hippocampus the two groups of animals were clearly separate. Towards the later

217 part of the intermediate hippocampus and into ventral hippocampus the brains were
218 indistinguishable, both being similar to control brains. This is consistent with the intended
219 location of the lesions, since far intermediate and ventral hippocampus were not targeted
220 (Table 1).

221 **Electrode localization**

222 Beyond just providing potentially useful landmarks, the skull also provides a stable structure to
223 support a microelectrode drive, thereby enabling minimal disruption of electrodes during
224 processing and scanning. Therefore, we evaluated if we could image functional electrodes
225 implanted in the brain and assess their location relative to brain structures. Independently
226 moveable tetrodes were implanted above dorsal and intermediate hippocampus. The
227 microdrive remained on the skull to minimally disrupt the electrodes. The brain, with skull and
228 microdrive intact, underwent imaging with micro-CT.

229 The electrodes were easily visualized, and the resolution was sufficiently fine to
230 distinguish the four individual electrodes that comprised each tetrode wire (Fig S2A). Although
231 the hardware used to stabilize the microdrive on the skull degraded the imaging quality
232 somewhat, there remained sufficient signal to resolve the pyramidal cell layer of the
233 hippocampus (Fig 4A). All that was required to identify individual electrodes was a visual
234 comparison of the layout of the canula of the drive and the arrangement of the electrodes from
235 the micro-CT (Fig 4B).

236 As with the lesions, here, with the electrodes, the goal is not just to visualize, but to also
237 extract relevant quantitative information. Again, it would be possible to perform image
238 segmentation for the hippocampal cell layer, but that would be quite laborious and subjective
239 at the most critical parts due to the large signal produced by the electrodes. Instead we sought
240 to extract coordinates that could form the basis of a systematic two-dimensional space on
241 which we could place the locations of the electrodes. For this analysis, we were most interested
242 in a two-dimensional space for the anterior-posterior and medial-lateral axis, since the
243 electrodes were moved over the course of the recording, thereby making the dorsal-ventral
244 coordinates of the CT not representative of the recording location.

245 We took advantage of the control brains that we scanned for the lesion cohort (n=12)
246 and utilized those brains to define a consistent two-dimensional coordinate system. As the
247 origin of the space we utilized the center of most anterior portion of the hippocampal CA1 cell
248 layer (Fig S2B). And then as point 1,1 we utilized the lateral extent of the hippocampal
249 (CA1/2/3) cell layer at the point where the dorsal and ventral portions of the hippocampus fuse
250 to form intermediate hippocampus (Fig S2B). We chose these points as they were easily visible
251 in all brains and would be likely visible in an electrode implanted brain as well. Within this
252 space, we then plotted, for each brain, sample locations of the lateral aspect of the
253 hippocampal cell layer and the medial aspect of the dentate gyrus cell layer from anterior to
254 posterior (Fig 4C&S2B). Across all brains the locations were very similar.

255 We then aligned the brain with the implanted electrodes to the same reference brain as
256 the lesion cohort and normalized the space by locating the equivalent points. In this
257 normalized space, the lateral aspect the hippocampal cell layer and the medial aspect of the

258 dentate gyrus cell layer fell within the range of the control brains, confirming the uniformity of
259 the space. This then allows for the placement of the anterior-posterior and medial-lateral
260 location of the electrodes (Fig 4C).

261 As the goal of localizing the electrodes is to inform the physiology recorded on those
262 electrodes, we took advantage of the finding of theta phase offset in the local field potential as
263 the hippocampus evolves along its septo-temporal axis (Lubenov and Siapas, 2009; Patel et al.,
264 2012). Within this two-dimensional space we confirmed a phase offset of the theta rhythm as
265 the hippocampus progress from dorsal to intermediate (Fig 4C&D) (see Materials and
266 Methods). Furthermore, this technique provides a straightforward reference to measure and
267 discover further axes along which such things could vary.

268

269 **Discussion**

270 We have presented a simple, cost-effective and scalable protocol for utilizing micro-CT to image
271 postmortem brain structure with the overlying skull (Fig 1 & Vid 1). The protocol allows for the
272 quantification of lesions (Fig 3) and localization of electrodes (Fig 4) within the brain. As
273 contrast for the micro-CT is provided by eosin, the processing for the presented protocol does
274 not preclude further histological sectioning and imaging of the brain (Fig 2).

275 This work builds upon the prior protocol that uses osmium as the contrast agent for
276 micro-CT (Masís et al., 2018), which allows for use with commercially available micro-CT
277 machines. Our protocol offers three key advantages over that previous protocol. First, our
278 protocol does not require multiple hazardous processing steps such as osmication, dehydration
279 and resin embedding—as described in Masís et al. (2018)—replacing it with a single step of 5%
280 eosin in water. Second, it allows for brain imaging with a partially intact skull, permitting the
281 direct measurement of skull landmarks relative to brain structures. If necessary, micro-CT of
282 the eosin-stained brain can also be done without a skull (data not shown). Third, our protocol
283 greatly simplifies the subsequent processing for histology as the tissue can be cut and stained
284 immediately after micro-CT with a range of standard histological stains. Our microscopic
285 analysis confirmed well-preserved neural morphology after incubation in 5% eosin (Fig 2). Our
286 protocol does, however, benefit from access to a synchrotron source to enable enough flux of
287 X-rays to allow for monochromatic and propagation phase contrast imaging. Although, there
288 are a limited number of synchrotrons, they are available to all.

289 Our protocol, while applied to the rat brain with a focus on the hippocampus, is
290 compatible with other species and other brain regions. With the expansion of organisms used
291 for genetic manipulations, neural recordings, and behavior this protocol can be very useful for
292 all stages of the process. Our protocol also presents an excellent way to quickly generate a
293 stereotactic atlas for guiding further experimentation. We note however, that micro-CT has
294 limitations on the maximal field of view available, making this methodology less appropriate for
295 larger brains.

296 There have been tremendous advances in recording technology to extract precise
297 quantitative physiological information from many regions and cells throughout the brain (J. E.
298 Chung et al., 2018; Jun et al., 2017; Voigts et al., 2020). However, the way in which we evaluate

the precise locations at which those devices recorded often rests on descriptive and qualitative metrics. Given the ever-expanding corpus of precise anatomical information, there is a need to improve the precision and quantitation of electrode locations, and our protocol provides such an approach. It also allows for rapid and more objective quantification of lesion extent and other features that one might wish to compare across brains.

Acknowledgements: We thank J Masis and A Joshi for helpful discussions. We thank H Barnard and A MacDowell for technical assistance. This work was supported by grants from the Jane Coffin Childs Memorial Fund for Medical Research (DBK), the UCSF Physician Scientist Scholars Program (DBK), an NIH R25 (R25MH060482) (DBK), an NIH Core Grant for Vision Research (NIH-NEI EY002162) (LDS), Research to Prevent Blindness (RPB Unrestricted Grant to the UCSF Department of Ophthalmology) (LDS) the Simons Foundation for Autism Research grant (291584) (LMF) and the Howard Hughes Medical Institute (LMF). This research used resources of the Advanced Light Source, a DOE Office of Science User Facility under contract no. DE-AC02-05CH11231.

Author contribution: DBK, VK and DYP conceived of the study. DBK, VK and DYP developed the protocol. DBK and DYP collected the data. DBK, RN, ZY and CS performed the surgeries. DBK, RN, LDS and LMF developed the analyses. DBK, RN, DAM, ZY, and GMW analyzed the data. DBK, VK, DYP and LMF wrote the paper.

Conflict of interest: VK is employed (part-time) by Neuralink Corp. The other authors declare no conflicts of interest.

Figure Legends:

Figure 1: micro-CT image of the intact brain with overlying skull. A) Three-dimensional representation of the overlying skull. B) The same brain and skull from A, virtually sliced along the sagittal plane (top), horizontal plane (bottom right) and coronal plane (bottom left).

Figure 2: Comparison of virtual slices to standard histological sections following Nissl (Cresyl Violet) stain. The same brain was utilized for both imaging modalities. A-E show different coronal slices along the anterior-posterior axis. Within each slice sample brain regions and anatomic landmarks that can be visualized both in the CT and Nissl stain are indicated using the brain atlas by Paxinos and Watson (2013).

Figure 3: Visualization and quantification of hippocampal lesions. A) Virtual coronal slice through example brains that underwent control surgery (left) and hippocampal lesion surgery (right). B) Example virtual slices of the hippocampus following aligning all brains and masking the hippocampus. Dorsal hippocampus is shown along the anterior-posterior axis and intermediate hippocampus is shown along the dorsal-ventral axis. Jagged edges seen in the dorsal-ventral slices reflect the fact that the mask was created and interpolated along the anterior-posterior axis. Scale bar applies to all images within this panel. C) Pairwise structural similarity metric (SSIM) between all pairs of brains. Each pixel represents the value of the SSIM averaged across all virtual slices bilaterally throughout the dorsal hippocampal formation and

339 the most dorsal part of the intermediate hippocampal formation. Matrix is ordered based on
340 the hierarchical cluster from panel D as indicated by the group labels at top. Dotted blue lines
341 demarcate the major groups from panel D. Left axis shows which are the control and lesion
342 brains. D) Dendrogram showing the results of the hierarchical clustering of all brain based on
343 the similarity matrix from panel C. Brains labeled as either control (C, black lines) or lesion (L,
344 green lines). E) Median (+- interquartile range) similarity of control (black) and lesion (green)
345 brains to intact brains as a function of anatomical location. Far left and far right plots show the
346 similarity metric calculated along the dorsal-ventral axis of the right and left
347 intermediate/ventral hippocampus, respectively. Middle left and middle right plots show the
348 similarity metric calculated along anterior-posterior axis of the right and left dorsal
349 hippocampus, respectively.

350 **Figure 4:** Visualization and quantification of electrode localization. A) Virtual coronal slice
351 through a brain with 22 tetrodes implanted, two of which can be visualized in the slice. B)
352 Virtual horizontal slice through the tetrodes (left). This image was processed to highlight the
353 tetrodes (see Table 2 for parameters). Image of the bottom of the canula of the drive implanted
354 into the brain (right) with the locations of the different tetrodes numbered. Xs indicate
355 locations that did not have tetrodes. C) Two-dimension coordinate system defined by the most
356 anterior part of the hippocampal cell layer (Fig S2B) and the lateral part of hippocampal cell
357 layer at the point of intermediate hippocampal fusion (Fig S2B). Left-most gray lines show the
358 locations of the medial part of dentate gyrus cell layer for 12 different brains. Rightmost gray
359 lines show the locations of the lateral part of the hippocampal cell layer. Diamonds demarcate
360 the same points for the electrode implanted brain. Circles represent the location of the
361 electrode implanted into the brain (one tetrode was utilized as reference and was therefore not
362 included in this plot). Colors within the circles show the mean phase offset of the theta rhythm
363 in the local field potential relative to the electrode denoted by the white circle. D) Example local
364 field potential recordings from electrodes from 4 different tetrodes with traces colored by the
365 phase offset. Black, top, trace is the reference electrode. Vertical dotted lines indicate the peak
366 of the theta rhythm in the reference (top) trace.

367 **Supplementary Figure 1:** Layout of micro-CT at the ALS. 1 indicated the location of the x-ray
368 source. 2 indicated the location of the sample, which rotates. 3 indication the location of the
369 collector optics.

370 **Supplementary Figure 2:** A) Fine scale tetrode structure can be visualized with the micro-CT.
371 Left shows a virtual horizontal slice, where the four individual electrodes that make up a single
372 tetrode can be seen. Right show a virtual coronal slice, where the individual electrode and the
373 braiding of the tetrode can be seen. B) Example brain showing the location of the coordinates
374 the make up the two-dimension space from Fig 4C. Virtual coronal slices of an example brain,
375 with sample points of the two-dimensional space demarcated as black dots. At AP=0 the dot
376 shows the origin point. At AP=1 the rightmost dot shows the point (1,1). For the rest of the
377 slices the rightmost dot shows the medial part of the dentate cell layer and the leftmost dot
378 shows the lateral aspect of the hippocampal cell layer. Scale bar applies to all images within the
379 panel.

380

AP (mm)	ML (mm)	DV (mm)
-2.8	±1.4	-3.0
-3.3	±2.4	-3.0
-4.1	±1.8	-2.8
-4.1	±3.4	-2.8
-4.8	±2.0	-2.8
-4.8	±4.2	-3.1
-5.5	±2.6	-3.0
-5.5	±3.6	-2.9
-5.5	±5.0	-3.5
-5.5	±5.0	-5.5
-6.2	±4.0	-3.4
-6.2	±5.4	-4.4

Table 1: Stereotaxic coordinates of NMDA infusions to produce lesions within the hippocampal formation. Adapted from Kim and Frank (2009). The coordinates are given for a Long Evans rat skull which is leveled so that bregma and lambda line in the same horizontal plane. AP: anteroposterior, ML: mediolateral, DV: dorsoventral. The AP and ML coordinates are measured from bregma. DV coordinates are measured from the dural surface above the brain.

	full brain (Fig 1&2)	lesion brains (Fig 3)	implant brain: electrodes (Fig 4)	implant brain: anatomy (Fig 4)
energy	25 keV	25 keV	25 keV	25 keV
angles	1313	1313	1313	1313
exposure	125 ms	100 ms	125 ms	125 ms
resolution	7.205 µm/pixel	7.84 µm/pixel	7.72 µm/pixel	7.72 µm/pixel
scintillator distance	540 mm	540 mm	540 mm	540 mm
# tiles	32	8	4	4
~scan time	150 min	32 min	25 min	25 min
outlier removal in 1d	true	true	False	true
ring removal	polar ring	polar ring	Fourier-wavelet	polar ring

max width for ring removal	100	100	100	200
min value of image to filter	0.5	0.6	-3000	0.6
max portion of image to filter	1.2	1.2	3000	1.2
manual centering	false	false	true	true
phase retrieval	true	true	false	true
alpha regularization	0.0005	0.0005	—	0.0005

Table 2: Scanning parameters and reconstruction parameters for Tomopy for all of the brains. The lesion brains include all of the brains described in Fig 3, including both the brains that underwent control and lesion surgery. The implanted brain was processed in two ways, one two resolve the brain anatomy and the other to maximally resolve the electrodes. The x-ray beam is only so wide; therefore, to scan an entire volume multiple tiles in the vertical dimension were taken and then the tiles were manually stitched together. The lesion brains were imaged from the striatum to the cerebellum to focus on the brain regions of interest and to save time.

Busse, M., Müller, M., Kimm, M.A., Ferstl, S., Allner, S., Achterhold, K., Herzen, J., Pfeiffer, F., 2018. Three-dimensional virtual histology enabled through cytoplasm-specific X-ray stain for microscopic and nanoscopic computed tomography. Proc Natl Acad Sci USA 115, 2293–2298. doi:10.1073/pnas.1720862115

Chung, K., Wallace, J., Kim, S.-Y., Kalyanasundaram, S., Andalman, A.S., Davidson, T.J., Mirzabekov, J.J., Zalocusky, K.A., Mattis, J., Denisin, A.K., Pak, S., Bernstein, H., Ramakrishnan, C., Grosenick, L., Gradinaru, V., Deisseroth, K., 2013. Structural and molecular interrogation of intact biological systems. Nature 497, 332–337. doi:10.1038/nature12107

Ding, Y., Vanselow, D.J., Yakovlevi, M.A., Katz, S.R., Lin, A.Y., Clark, D.P., Vargas, P., Xin, X., Copper, J.E., Canfield, V.A., Ang, K.C., Wang, Y., Xiao, X., De Carlos, F., van Rossum, D.B., La Riviere, P., Cheng, K.C., 2019. Computational 3D histological phenotyping of whole zebrafish by X-ray histotomograhpy. Elife 8. doi:10.7554/eLife.44898

Dyer, E.L., Gray Roncal, W., Prasad, J.A., Fernandes, H.L., Gürsoy, D., De Andrade, V., Fezzaa, K., Xiao, X., Vogelstein, J.T., Jacobsen, C., Kording, K.P., Kasthuri, N., 2017. Quantifying Mesoscale Neuroanatomy Using X-Ray Microtomography. eNeuro 4. doi:10.1523/ENEURO.0195-17.2017

Fedorov, A., Beichel, R., Kalpathy-Cramer, J., Finet, J., Fillion-Robin, J.-C., Pujol, S., Bauer, C., Jennings, D., Fennessy, F., Sonka, M., Buatti, J., Aylward, S., Miller, J.V., Pieper, S., Kikinis, R.,

2012. 3D Slicer as an image computing platform for the Quantitative Imaging Network. Magn Reson Imaging 30, 1323–1341. doi:10.1016/j.mri.2012.05.001

Hatta, H., Tsuneyama, K., Nomoto, K., Hayashi, S., Miwa, S., Nakajima, T., Nishida, T., Nakanishi, Y., Imura, J., 2014. A simple and rapid decalcification procedure of skeletal tissues for pathology using an ultrasonic cleaner with D-mannitol and formic acid. Acta Histochem. 116, 753–757. doi:10.1016/j.acthis.2014.01.006

Kikinis, R., Pieper, S.D., Vosburgh, K.G., 2014. 3D Slicer: A Platform for Subject-Specific Image Analysis, Visualization, and Clinical Support, in: Intraoperative Imaging and Image-Guided Therapy. Springer, New York, NY, New York, NY, pp. 277–289. doi:10.1007/978-1-4614-7657-3_19

Kim, S.M., Frank, L.M., 2009. Hippocampal lesions impair rapid learning of a continuous spatial alternation task. PLoS One 4, e5494. doi:10.1371/journal.pone.0005494.t001

Lubenov, E.V., Siapas, A.G., 2009. Hippocampal theta oscillations are travelling waves. Nature 459, 534–539. doi:10.1038/nature08010

Masís, J., Mankus, D., Wolff, S.B.E., Guitchounts, G., Joesch, M., Cox, D.D., 2018. A micro-CT-based method for quantitative brain lesion characterization and electrode localization. Sci Rep 8, 5184. doi:10.1038/s41598-018-23247-z

Müller, M., Kimm, M.A., Ferstl, S., Allner, S., Achterhold, K., Herzen, J., Pfeiffer, F., Busse, M., 2018. Nucleus-specific X-ray stain for 3D virtual histology. Sci Rep 8, 17855. doi:10.1038/s41598-018-36067-y

Patel, J., Fujisawa, S., Berényi, A., Royer, S., Buzsáki, G., 2012. Traveling theta waves along the entire septotemporal axis of the hippocampus. Neuron 75, 410–417. doi:10.1016/j.neuron.2012.07.015

Paxinos, G., Watson, C., 2013. The Rat Brain in Stereotaxic Coordinates. Academic Press.

Renier, N., Wu, Z., Simon, D.J., Yang, J., Ariel, P., Tessier-Lavigne, M., 2014. iDISCO: a simple, rapid method to immunolabel large tissue samples for volume imaging. Cell 159, 896–910. doi:10.1016/j.cell.2014.10.010

Savi, F.M., Brierly, G.I., Baldwin, J., Theodoropoulos, C., Woodruff, M.A., 2017. Comparison of Different Decalcification Methods Using Rat Mandibles as a Model. J. Histochem. Cytochem. 65, 705–722. doi:10.1369/0022155417733708

Schindelin, J., Arganda-Carreras, I., Frise, E., Kaynig, V., Longair, M., Pietzsch, T., Preibisch, S., Rueden, C., Saalfeld, S., Schmid, B., Tinevez, J.-Y., White, D.J., Hartenstein, V., Eliceiri, K., Tomancak, P., Cardona, A., 2012. Fiji: an open-source platform for biological-image analysis. Nat Methods 9, 676–682. doi:10.1038/nmeth.2019

Schindelin, J., Rueden, C.T., Hiner, M.C., Eliceiri, K.W., 2015. The ImageJ ecosystem: An open platform for biomedical image analysis. Mol. Reprod. Dev. 82, 518–529. doi:10.1002/mrd.22489

Schneider, C.A., Rasband, W.S., Eliceiri, K.W., 2012. NIH Image to ImageJ: 25 years of image analysis. Nat Methods 9, 671–675. doi:10.1038/nmeth.2089

Wang, Z., Bovik, A.C., 2009. Mean Squared Error: Love It or Leave It? A new look at signal fidelity measures. Ieee Signal Processing Magazine 26, 98–117. doi:10.1109/MSP.2008.930649

Wang, Z., Bovik, A.C., Sheikh, H.R., Simoncelli, E.P., 2004. Image quality assessment: from error visibility to structural similarity. IEEE Trans Image Process 13, 600–612. doi:10.1109/tip.2003.819861

Figure 1

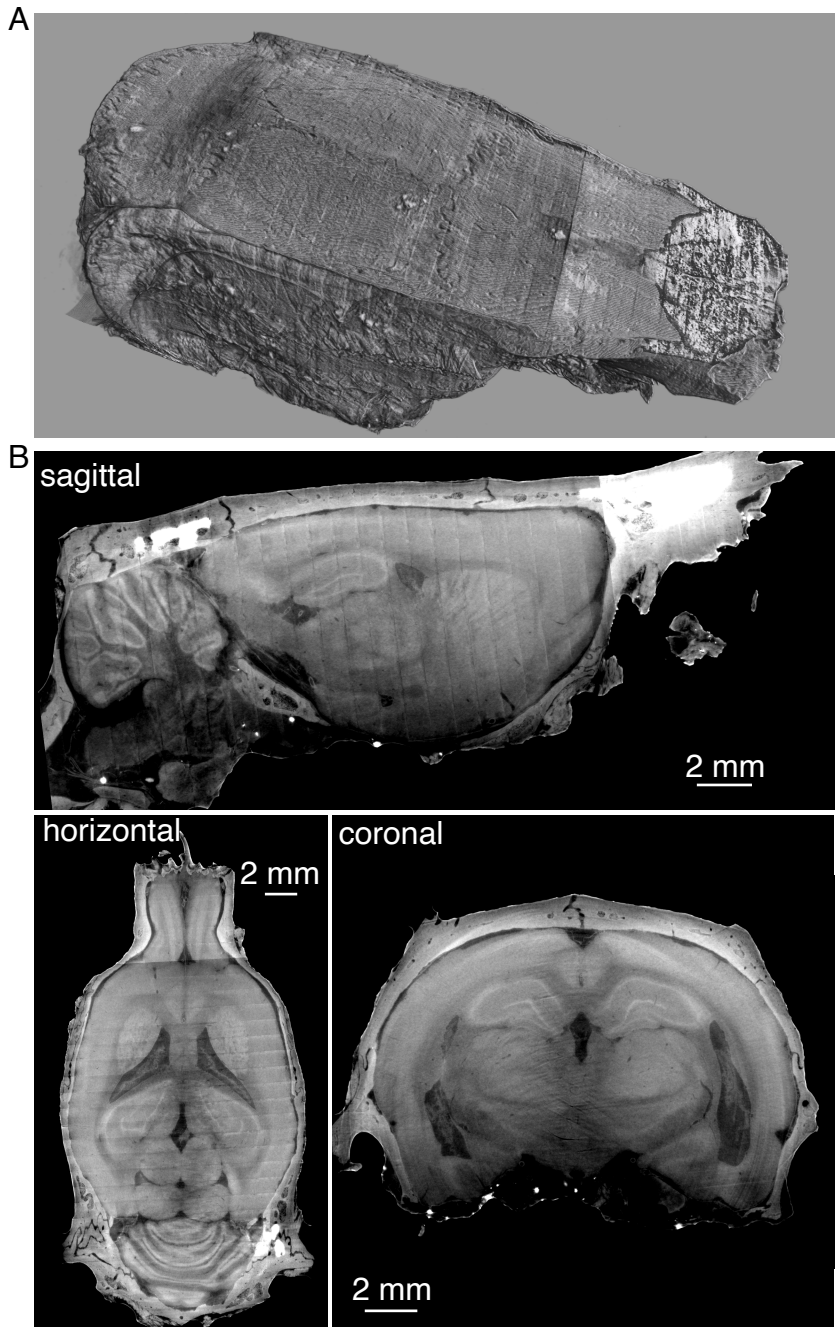

Figure 2

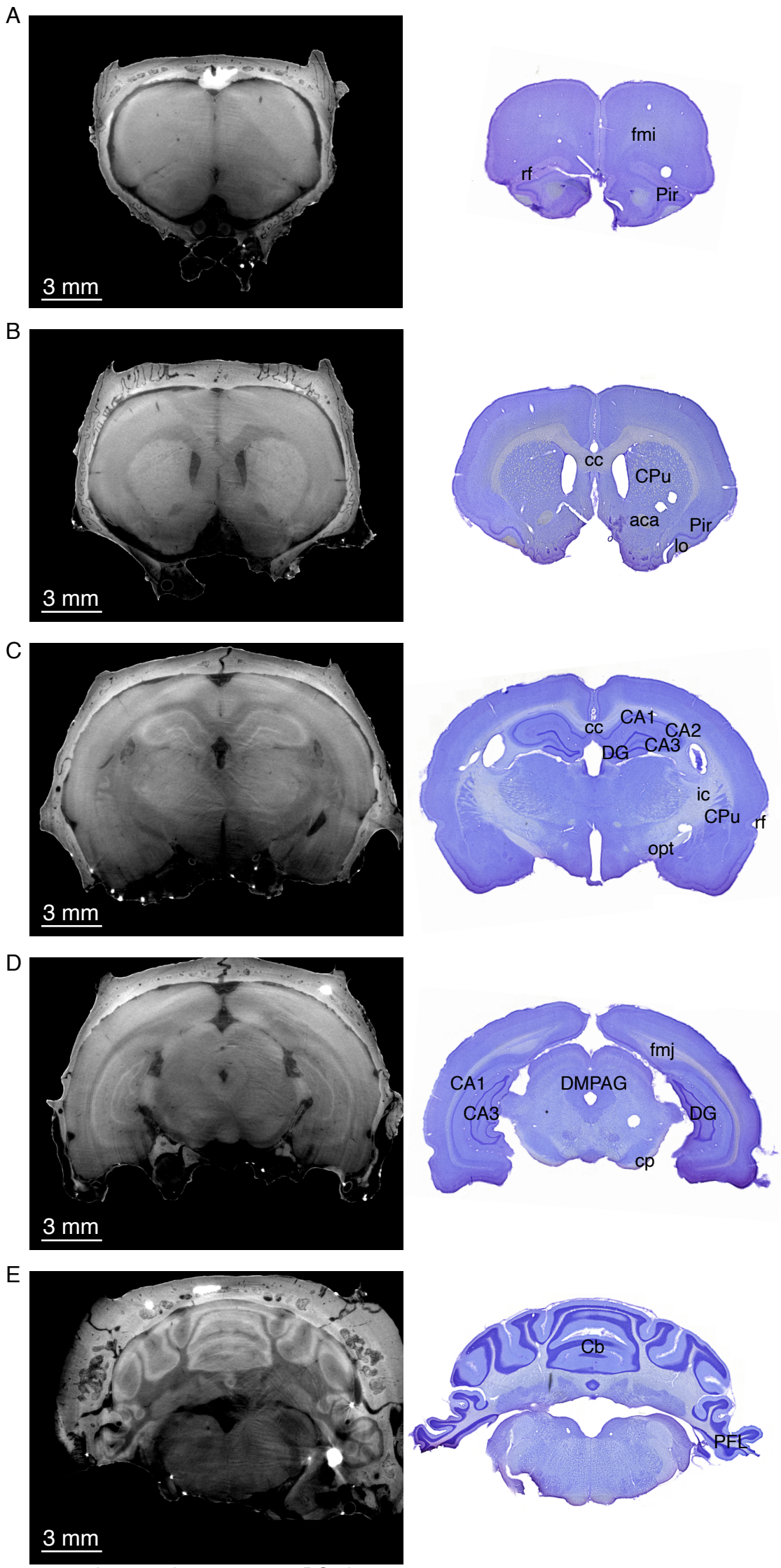

aca: anterior commissure, ant
CA1/2/3: hippocampal cell layer
Cb: cerrebellar lobules
cc: corpus callosum
cp: cerebral peduncle
CPu: caudate putamen (striatum)
DG: dentate gyrus
DMPAG: dorsomedial periaqueductl grey
fmi: forceps minor corpus callosum
fmj: forceps major corpus callosum
ic: internal capsule
lo: lateral olfactory tract
opt: optic tract
PFl: paraflocculus
Pir: piriform cortex
rf: rhinal fissure

Figure 3

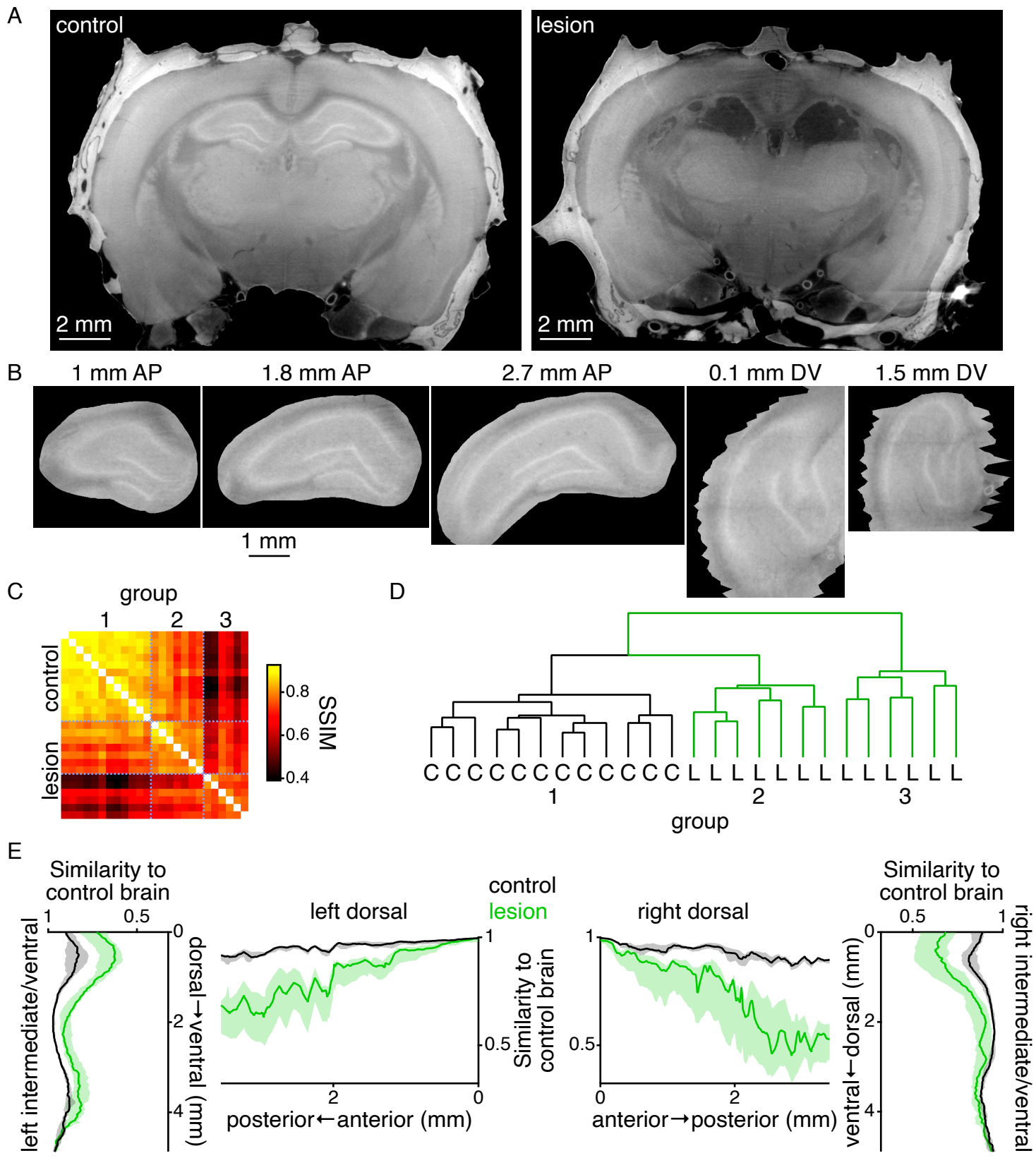
A
control
2 mm
lesion
2 mm
B
1 mm AP
1.8 mm AP
2.7 mm AP
0.1 mm DV
1.5 mm DV
1 mm
C
group
1
2
3
control
lesion
0.8
0.6
0.4
SSIM
D
C C C C C C C C C C C C C L L L L L L L L L L L L L
1
2
3
group
E
Similarity to control brain
1
0.5
0
2
4
left intermediate/ventral
dorsal→ventral (mm)
left dorsal
control
lesion
1
0.5
Similarity to control brain
2
0
posterior←anterior (mm)
right dorsal
1
0.5
0
2
anterior→posterior (mm)
Similarity to control brain
0.5
1
0
2
4
ventral←dorsal (mm)
right intermediate/ventral

Figure 4

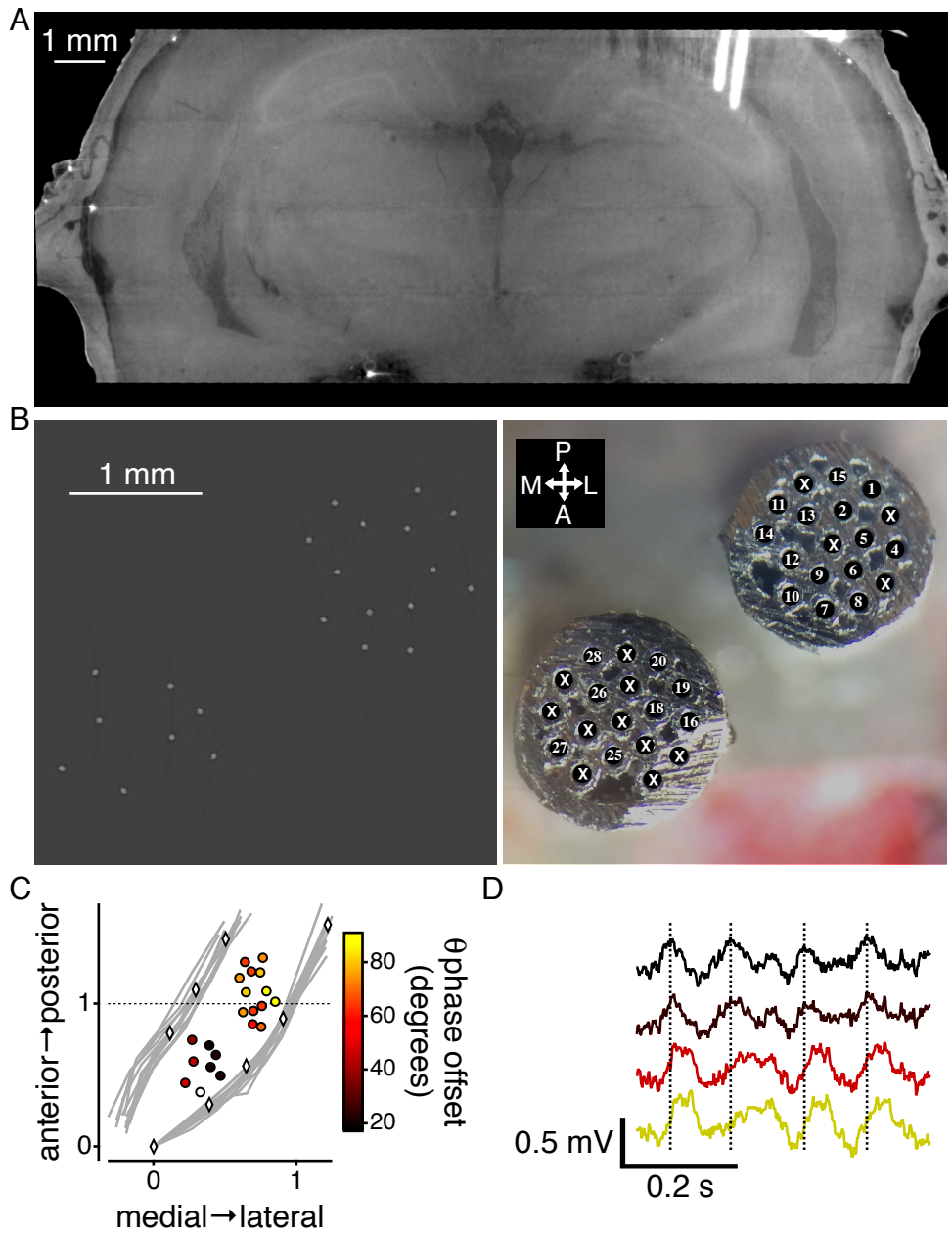
A
1 mm
B
1 mm
P
M
L
A
C
anterior→posterior
medial→lateral
0
1
0
1
θ phase offset (degrees)
80
60
40
20
D
0.5 mV
0.2 s

Supplementary Figure 1

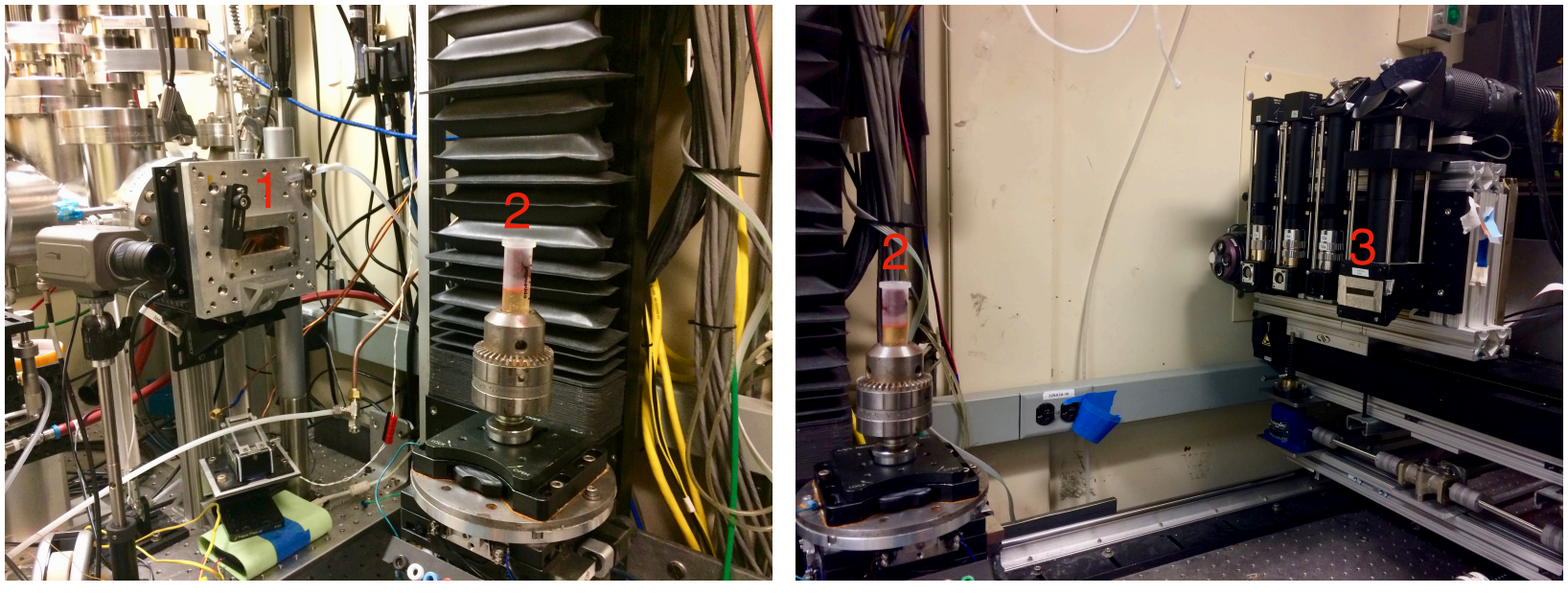
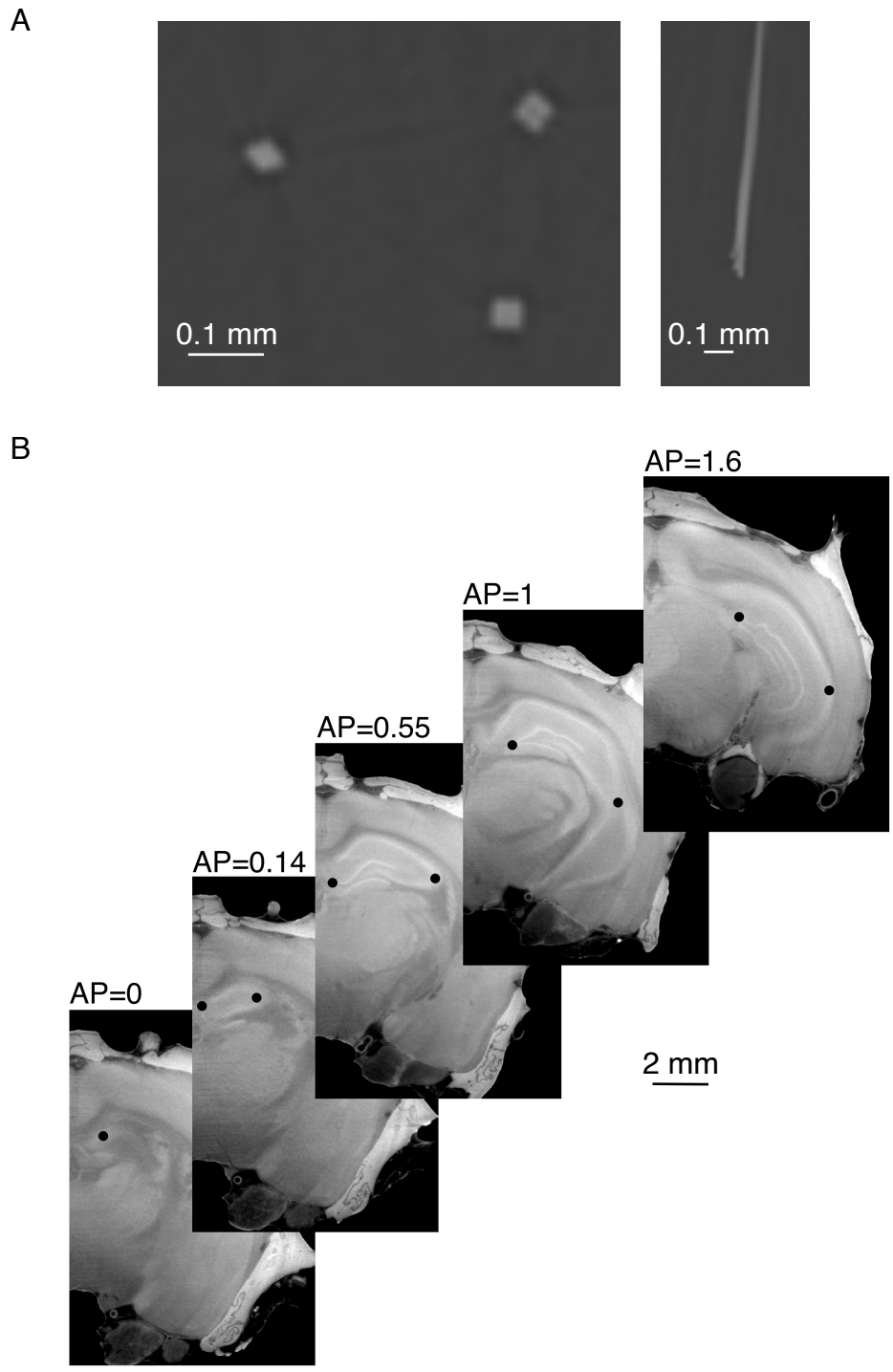
Supplementary Figure 2